Nanoscale

PAPER

View Article Online
View Journal | View Issue

Cite this: *Nanoscale*, 2025, **17**, 14696

Activated carbon derived from shrimp waste enhanced by ball milling: a green solution for CO_2 capture and waste valorization

Haif Aljomard, *[a,b] Omar Awayssa[c] and Chaouki Ghenai [a,d]

Received 18th February 2025,
Accepted 13th May 2025

DOI: 10.1039/d5nr00725a

rsc.li/nanoscale

Shrimp waste-derived biochar (BC), pretreated with HCl, was chemically activated with KOH at varying mass ratios and subjected to ball milling to engineer high-performance CO_2 adsorbents. Comprehensive characterization, including TGA, BET surface area analysis, DLS zeta potential, FT-IR, FE-SEM, and EDS, revealed significant structural enhancements. Textural analysis showed a dramatic surface area increase from 3 m^2 g^{-1} for raw biochar to 924.4 m^2 g^{-1} for the T-AC1:2 sample (HCl-treated BC and KOH-activated at a 1 : 2 ratio). The optimized sample, n-T-AC1:1 (HCl-treated, KOH-activated 1 : 1, and ball-milled), achieved the highest CO_2 adsorption capacity of 5.14 mmol g^{-1} at 0 °C and 1 bar. Nonlinear isotherm modeling indicated Freundlich behavior at 0 °C and Redlich–Peterson behavior at 25 °C and 40 °C, while thermodynamic analysis confirmed spontaneous, exothermic physisorption. The optimized adsorbent also demonstrated excellent cycling stability over multiple adsorption–desorption cycles, confirming its regeneration potential. These findings demonstrate that the shrimp waste valorization strategy, combined with chemical and mechanical treatments, offers a scalable and sustainable route for developing high-performance carbon capture materials, contributing to waste reduction and climate change mitigation.

1. Introduction

In recent years, the generation of shrimp waste (SW) has experienced rapid and significant growth, driven by the expanding global shrimp production industry.[1–3] In 2023, global shrimp production reached 5.6 million tons, with projections indicating growth to 7.28 million tons by 2025. This expansion has significantly increased shrimp waste generation, with more than half of the total catch typically becoming by-products. Around 3.8 million tons of shrimp waste are produced annually, primarily from the head and tail, which account for a substantial portion of the shrimp's total weight. Asia, as the leading shrimp producer, accounts for 70% of the global market share. Shrimp processing generates by-products that make up 40–60% of the total mass, with shrimp heads constituting 40–48% of this waste, often discarded unless repurposed for other applications.[4,5] Improper disposal of SW leads to foul odors and the spread of infectious diseases through pests, resulting in significant environmental pollution. This threatens local ecosystems and livelihoods, highlighting the urgent need for sustainable waste management solutions.[6–8] However, SW is more than just a waste product; it is a resource rich material containing valuable micronutrients and bioactive compounds like proteins, lipids, chitin/chitosan, enzymes, pigments, minerals, vitamins, and calcium carbonate, all of which hold significant commercial potential.[9–14] Since there has been a growing emphasis on environmental sustainability and resource optimization, managing these by-products has become increasingly important.[15,16] Among these bioactive components, chitin, a naturally occurring biopolymer abundant in shrimp shells, and its derivative chitosan stand out due to their remarkable antibacterial properties. They are effective against a wide range of human, food, and waterborne pathogens, which makes them highly valuable in diverse applications such as water treatment, food preservation, biomedical fields, and even as organic fertilizers in agriculture.[17–20] In addition to these applications, SW and its derived biochar are gaining popularity in crop cultivation as rich sources of essential nutrients that promote healthy plant growth.[21,22] Beyond this, the integration of biochar technology and nanobiotechnology is paving the way for the development of carbon-based nanomaterials, including nano-biochar and biochar nanocomposites, which are revolutionizing research in this area. The advances in nanotechnology allow biochar particles to be reduced, significantly enhancing properties like

[a]*Biomass and Bioenergy Research Group, Center for Sustainable Energy and Power Systems Research, Research Institute of Sciences and Engineering, University of Sharjah, Sharjah, United Arab Emirates. E-mail: haifaljomard@gmail.com*
[b]*Department of Chemistry, College of Sciences, Mosul University, Mosul 41002, Iraq*
[c]*Department of Chemical and Petroleum Engineering, UAEU, 15551 Al Ain, United Arab Emirates*
[d]*Department of Sustainable and Renewable Energy Engineering, University of Sharjah, Sharjah, United Arab Emirates*

porosity, surface area, and mobility. Superior plant growth, soil quality, and pollution cleanup are just a few of the many advantages of nano-biochar compared to traditional biochar. It is also effective in wastewater treatment, enzyme immobilization, and carbon sequestration, positioning it as a sustainable and cost-effective alternative for environmental applications, thus contributing to climate change mitigation.[23–25] A promising approach for converting seafood waste into sustainable carbon precursors aligns with green synthesis principles, utilizing the abundant and low-cost nature of SW. This transformation not only reduces environmental impact but also allows for surface modifications tailored for diverse applications, presenting a sustainable pathway for waste valorization and advancing nanotechnology.[26,27] Engineered biochar, a carbon-rich solid derived from biomass or waste materials through pyrolysis, is further enhanced through modification techniques such as chemical, physical, or biological treatment. This type of biochar boasts a higher specific surface area, adsorption capacity, and cation exchange capacity compared to traditional biochar, making it ideal for various applications.[28]

Ball milling is an efficient and reproducible mechanochemical process used for biochar modification and functionalization, converting it into value-added, eco-friendly products. This technique involves grinding biochar to adjust key characteristics such as particle size, specific surface area, and oxygenated functional groups, which in turn enhances adsorption and catalytic performance.[29] By utilizing mechanical energy, ball milling alters the chemical and structural properties of materials, making it highly effective and environmentally friendly. The high-speed rotation of the mill generates activation energy, which induces chemical reactions that modify the material properties, resulting in powders with improved physical, chemical, and mechanical characteristics.[30] Moreover, the simplicity, energy efficiency, and sustainability of ball milling make it a preferred method for material mixing and size control. The process is influenced by key parameters like milling time and rotation speed, which directly affect the morphology and porosity of carbon materials, ultimately enhancing their structural properties.[31] Additionally, integrating nanoparticles into carbon-based materials through ball milling has proven to be a cost-effective strategy for producing high-performance nanocomposites with enhanced surface characteristics.[32] Building upon advanced modification techniques, the originality of this study lies in its comparative analysis of chemical treatment and mechanical ball milling on both biochar and activated carbon derived from shrimp waste. Potassium hydroxide (KOH) is a widely recognized activating agent for developing carbon materials with high microporosity and large surface areas, key features for effective CO_2 adsorption.[33] Nevertheless, despite its effectiveness in tuning porosity and surface chemistry, KOH activation presents notable drawbacks, including corrosiveness, equipment degradation, and environmental concerns.[34] Despite its corrosive nature, which understandably raises environmental and handling concerns, KOH remains one of the most widely used and reliable activating agents in carbon material synthesis.[35] In this study, we addressed these limitations by applying moderate KOH to precursor ratios and implementing extensive post-synthesis washing protocols to remove residual chemicals and neutralize pH. This practical balance between activation efficiency and sustainability allowed us to harness the performance advantages of KOH activation while minimizing its environmental impact, ensuring a more sustainable preparation route. KOH activation has also been widely reported as one of the most effective strategies to improve CO_2 selectivity, owing to the chemically alkaline surface. This alkaline environment strengthens the interactions between basic surface groups and acidic CO_2 molecules. Furthermore, potassium species can diffuse into the carbon matrix, promoting pore widening and improving the accessibility of adsorption sites. These structural and surface modifications collectively contribute to improved CO_2 uptake performance of biochar activated by KOH.[36,37] Utilizing KOH as the activating agent at varying mass ratios, we systematically investigate how these treatments influence the structural, morphological, and adsorption properties of HCl-treated carbon materials, with particular emphasis on enhancing CO_2 capture performance. Despite significant advances in carbon capture materials, the sustainable valorization of marine biowaste into functional adsorbents remains largely underexplored. This study introduces a structured approach to engineer high-performance CO_2 adsorbents from shrimp waste-derived biochar, integrating chemical activation (HCl pretreatment and KOH activation) with mechanical ball milling to tailor both the textural properties and surface chemistry. Unlike conventional biomass-derived carbons, the synergistic combination of acid–base modification and mechanical treatment applied here offers a scalable pathway to produce nano-activated carbon with enhanced CO_2 uptake, surface reactivity, and regeneration stability. The novelty of this work lies in: (i) the combined use of chemical activation and mechanical ball milling to engineer functional nanocarbon from shrimp waste, (ii) the detailed investigation of adsorption mechanisms using nonlinear modeling and thermodynamic analysis to confirm multilayer physisorption behavior, and (iii) the demonstration of excellent cyclic regeneration stability of the optimized material after long-term storage, highlighting its promising potential for future real-world carbon capture applications. Overall, this study introduces a scalable and sustainable pathway for converting marine biowaste into high-performance carbon materials, contributing meaningfully to climate change mitigation and circular economy initiatives.

2. Materials and methods

2.1 Materials

The heads and shells of white shrimp, identified as SW, were sourced from Souq Al Jubail, Sharjah, with the shrimp originating from Oman. The material was thoroughly washed with deionized water to eliminate impurities, air-dried at 65 °C over-

night, and subsequently crushed, ground, and sieved to achieve a particle size of less than 125 μm. Potassium hydroxide (KOH), 85–100% purity (Sigma-Aldrich, USA), and hydrochloric acid (HCl), 37% concentration (Merck, Austria), were used without further purification.

2.2 Synthesis of shrimp waste-derived biochar

SW-derived biochar was synthesized *via* slow pyrolysis in a fixed-bed reactor (BFK-1.0L reactor, China).[38,39] A 50 g sample of SW powder was placed in the reactor and carbonized at 500 °C under a nitrogen atmosphere, using a heating rate of approximately 7 °C min^{-1} and a residence time of 2 h.[40,41] The resulting biochar was labeled as BC. To remove impurities such as $CaCO_3$, $MgCO_3$, and MgO, BC underwent chemical treatment with a 3 mol L^{-1} hydrochloric acid (HCl) solution. The mixture was stirred for 6 h, filtered, and washed with deionized water until neutral pH was achieved.[13,42] Finally, the treated biochar was dried at 65 °C for 12 h and labeled as T-BC.

2.3 Synthesis of shrimp waste-derived activated carbon

Activated carbon (AC) was synthesized using two methods: non-chemical treatment and chemical treatment with HCl. In the non-chemical treatment method, SW raw material was ground into powder and dry mixed with KOH at mass ratios of 1 : 1, 1 : 2, and 1 : 3. These mixtures were subjected to a one-step carbonization and activation process at 500 °C in a fixed bed reactor,[40] under the pyrolysis conditions specified in section 2.2. The resulting AC samples, denoted as AC1:1, AC1:2, and AC1:3, were thoroughly washed with deionized water using centrifugation and vacuum filtration until neutral pH was reached, followed by drying at 65 °C for 12 h. In the chemical treatment method, BC carbonized at 500 °C was pre-treated with HCl to produce T-BC, which was then dry mixed with KOH at mass ratios of 1 : 1 and 1 : 2. These mixtures were activated at 800 °C in a nitrogen atmosphere furnace, with a heating rate of 20 °C min^{-1} and a residence time of 1 h, producing samples labeled as T-AC1:1 and T-AC1:2. All samples were subsequently subjected to ball milling to achieve nanoscale dimensions, for CO_2 capture applications.

2.4 Yield calculation

The yield percentage of biochar (BC) was calculated using eqn (1) as follows[43] :

$$\text{Yield}\,(\%) = \frac{W_f}{W_i} \times 100 \quad (1)$$

where W_f represents the final BC mass (g), and W_i denotes the initial dry mass (g) of SW.

Furthermore, the yield percentages of activated carbon (AC) and treated activated carbon (T-AC) samples were calculated after washing, as outlined in eqn (2):[44]

$$\text{Yield}\,(\%) = \frac{W_C}{W_i} \times 100 \quad (2)$$

In this equation, W_i represents the initial dry mass of SW mixed with KOH, while W_c denotes the final mass of the AC samples labelled as AC1:1, AC1:2, and AC1:3. For the treated samples, W_i corresponds to the mass of T-BC dry mixed with KOH at ratios of 1 : 1 and 1 : 2, respectively, while W_c represents the final mass of the T-AC samples, T-AC1:1 and T-AC1:2.

2.5 Mechanical method

The mechanical processing involved placing 1 g of each carbon sample (both with and without chemical treatment) into a 25 mL corundum jar, along with seven 4 mm corundum balls, maintaining a biochar to ball mass ratio of 1 : 28. Using a planetary ball mill (PM100, Retsch Corporation, Germany), the samples were milled at 500 rpm for 2 h at room temperature, with the rotation direction reversed every 15 min to regulate temperature and improve milling efficiency.[45] Following milling, the samples were sonicated for 30 min using a Branson Ultrasonic Cleaner (Model 2510R-DTH, USA). Centrifugation was then conducted for 10 min using a Hettich MIKRO 220R microliter centrifuge, followed by filtration, as illustrated in (Fig. 1). Finally, the samples were dried at 65 °C for 12 h, producing nanoscale products labeled as n-samples, such as n-BC, n-T-BC, n-AC1:1, T-n-AC1:1, and other corresponding carbon samples.

2.6 Characterization of carbon samples

Thermal stability was assessed through thermogravimetric analysis (TGA) with an STA 449 Jupiter F5 analyzer (NETZSCH, Germany), specifically for the SW raw material. The higher heating value (HHV) of SW and SW derived biochar was measured using a Parr 6400 calorimeter. To comprehensively analyze the structural and surface properties of the BC and AC derived SW samples, both before and after chemical/mechanical treatment, a range of advanced characterization techniques were utilized. Functional groups in the samples were identified using Fourier Transform Infrared (FTIR) spectroscopy (JASCO FTIR-6300, Japan), with spectra recorded over a wavelength range of 500–4000 cm^{-1}, after mixing activated carbon with KBr and forming into pellets, which were then fed into the instrument. Surface morphology and chemical composition were examined using Field Emission Scanning Electron Microscopy (FE-SEM, Apreo, Thermo-Fisher Scientific, USA) coupled with Energy Dispersive Spectroscopy (EDS, Bruker

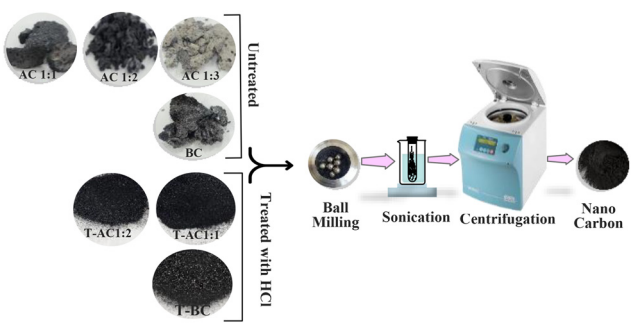

Fig. 1 Mechanical processing applied to SW derived BC and AC samples.

XFlash 6/60, Germany). Textural properties, BET surface area and BJH Pore Size Distribution (PSD) were determined *via* nitrogen adsorption/desorption analysis using a NOVATECH LX2 analyzer (Anton Paar, Austria). Additionally, the zeta potentials of the synthesized BC and AC samples were measured at 25 °C through dynamic light scattering (DLS) using a Litesizer 500 (Anton Paar, Austria).

The CO_2 adsorption capacity was measured using a NOVATECH LX2 analyzer (Anton Paar, Austria) at 0 °C using an external circulating water bath (JULABO 200F) over a pressure range of 0 to 1 bar. Before each adsorption test, all carbon samples both before and after chemical/mechanical treatment were degassed at 250 °C for 6 h under vacuum to remove any residual moisture. After cooling to the desired temperature, only CO_2 with a high purity of 99.9% was introduced into the system for adsorption analysis.

2.7 Adsorption isotherms

Carbon dioxide adsorption behavior at 0 °C, 25 °C, and 40 °C was evaluated using five distinct isotherm models: Langmuir, Freundlich, Toth, Sips, and Redlich–Peterson. These include two-parameter models (Langmuir, Freundlich) and three-parameter models (Redlich–Peterson, Toth, and Sips), which were applied to interpret the experimental CO_2 adsorption data on activated carbon and gain insights into adsorption mechanisms.[46] The non-linear equations representing these models are detailed in Table 1.

The parameters used in these non-linear isotherm model equations are as follows: P represents the relative pressure of the adsorbate (bar), while q_e denotes the equilibrium adsorbed amount (mmol g^{-1}), and q_m is the maximum adsorption capacity (mmol g^{-1}). K_L is the Langmuir isotherm constant (bar^{-1}), K_F is the Freundlich isotherm constant (bar^{-1}), K_T is the Toth isotherm constant (bar^{-1}), K_{RP} is the Redlich–Peterson isotherm constant (bar^{-1}), and K_s is the Sips isotherm constant (bar^{-1}). The heterogeneity factors are represented as $1/n_F$ for the Freundlich model and n_T for the Toth model, respectively, while n_s is the Sips isotherm exponent. Finally, a_{RP} is a constant (bar^{-1}) and β_{RP} is the Redlich–Peterson isotherm exponent.

Table 1 Non-linear isotherm models for CO_2 adsorption

Model	Equations	Ref.
Langmuir	$q_e = q_m \frac{K_L \cdot P}{(1 + K_L \cdot P)}$	47
Freundlich	$q_e = K_F \times P^{\frac{1}{n_F}}$	48
Toth	$q_e = \frac{q_m \times K_T \times P}{\left[1 + (K_T \times P)^{n_T}\right]^{\frac{1}{n_T}}}$	49
Sips	$q_e = \frac{q_m \times (K_S \times P)^{\frac{1}{n_s}}}{1 + (K_S \times P)^{\frac{1}{n_s}}}$	50
Redlich–Peterson	$q_e = \frac{K_{RP} \times P}{1 + a_{RP} \times P^{\beta_{RP}}}$	51

2.8 Adsorption thermodynamics

Thermodynamic properties are fundamental in evaluating adsorption processes, particularly in determining their spontaneity. Changes in free energy ($\Delta G°$), entropy ($\Delta S°$), and enthalpy ($\Delta H°$) provide critical insights into the feasibility and intrinsic nature of CO_2 adsorption on activated carbon.[52] A negative $\Delta G°$ value indicates that the process is thermodynamically favorable and occurs spontaneously at a given temperature. The magnitude of $\Delta G°$ also reflects the energy efficiency of the process. The enthalpy change $\Delta H°$ determines whether the adsorption is exothermic $\Delta H° < 0$ or endothermic $\Delta H° > 0$. Meanwhile, a positive $\Delta S°$ value signifies an overall increase in randomness and highlights the affinity between the adsorbent and adsorbate.[53]

These thermodynamic parameters were calculated using eqn (3)–(5). Specifically, $\Delta G°$ was directly obtained from eqn (3), while $\Delta H°$ and $\Delta S°$ were determined from the slope and intercept of the van't Hoff plot ($\ln K_d$ *versus* $1/T$) using eqn (4). In this context, R represents the universal ideal gas constant (8.314 J mol^{-1} K), and T is the absolute temperature (K).[54,55] By integrating these equations, the calculations of thermodynamic parameters offer comprehensive insights into the energy- and entropy-related aspects of the adsorption mechanism, as detailed in the following equations:[56]

$$\Delta G° = -RT \ln K_d \quad (3)$$

$$\ln K_d = \frac{\Delta S°}{R} - \frac{\Delta H°}{RT} \quad (4)$$

$$K_d = \frac{q_e}{P} \quad (5)$$

3. Results and discussion

3.1 TGA/DTG and HHV analysis of SW

The thermal decomposition behavior of SW was evaluated through proximate analysis, revealing distinct thermal events aligned with its composition. The initial mass loss, representing 4.80% moisture, occurred at around 105 °C. This was followed by the release of volatile matter, constituting 70.48%, at approximately 550 °C, and a residual ash content of 5.79% remained up to 800 °C, as well as a fixed carbon content of 18.19%, consistent with previous findings.[57] The TGA profile of the raw SW material is presented in Fig. 2. The derivative thermogravimetric (DTG) curve highlights the rate of mass loss across various temperature ranges, with a pronounced peak observed at around 500 °C. This indicates an optimal temperature range for pyrolysis between 400 °C and 600 °C.[58] This TGA/DTG analysis of shrimp waste is crucial for optimizing pyrolysis and carbonization processes, as it identifies critical temperature ranges necessary for the decomposition of various constituents and the subsequent formation of biochar or activated carbon. In addition to thermal analysis, the Higher Heating Values (HHVs) of SW and its derived BC were measured to assess energy potential. The HHV of raw SW was

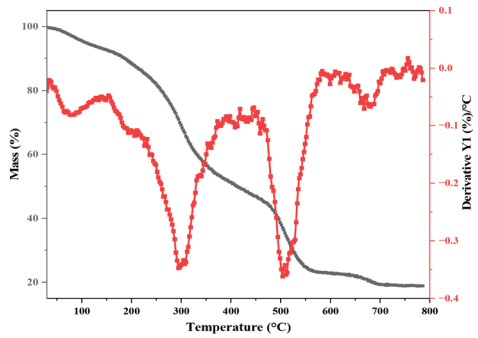

Fig. 2 Thermogravimetric analysis of SW conducted at a constant heating rate of 20 °C min^{-1} under an air atmosphere, utilizing a sample mass of 38.8 mg.

found to be 16.44 MJ kg^{-1}, whereas the HHV of SW-derived biochar increased to 20.64 MJ kg^{-1}, closely aligning with values reported in previous studies.[59] This improvement provides a benchmark for evaluating the energy efficiency of the conversion process.

3.2 N_2 adsorption isotherms, surface area and porosity

The surface area and porosity of BC and AC derived from SW exhibit notable changes after ball milling, influencing their adsorption capabilities. For biochar, ball milling significantly enhances porosity, increasing the surface area from 3 m^2 g^{-1} to 47 m^2 g^{-1}, while the pore volume expands from 0.012 cm^3 g^{-1} to 0.088 cm^3 g^{-1}. Additionally, the pore radius decreases from 8.25 nm to 3.73 nm. In the case of activated carbon, the KOH to SW ratio plays a crucial role in determining structural changes. For AC1:1, the surface area decreases from 164 to 65 m^2 g^{-1}, with a notable drop in the pore volume from 0.391 to 0.114 cm^3 g^{-1} and a reduced pore size. A similar trend is observed for AC1:2, where the surface area drops from 124 to 20 m^2 g^{-1}, with an expansion in the pore radius, suggesting partial structural collapse or pore blockage. Meanwhile, AC1:3 exhibits reductions in both surface area and pore volume, coupled with an increase in the pore radius. To further understand these changes, the mesopore volume (V_{Meso}) is determined by subtracting the micropore volume (V_{mic}) from the total pore volume (V_t).[43] As detailed in Table 2, the results reveal a contrasting effect of ball milling: while it enhances biochar porosity, it alters the structure of activated carbon, impacting its adsorption performance. This may be attributed to some structural deformations that could have limited pore accessibility, which implies a reduction in the adsorption capacity. The noticeable reduction in the surface area of the sample T-AC1:1 after ball milling from 711 to 240 m^2 g^{-1} can be attributed to the agglomeration of ultrafine particles and partial pore collapse, both of which are commonly observed effects of high-energy mechanical processing. During ball milling, intensive shear and compressive forces promote particle fusion and compaction, which may lead to the blockage or deformation of internal pore structures. This outcome has been similarly reported by Nasrullah *et al.*[60] and supported by the findings of Ryu and Lee.[61] These observations highlight the importance of optimizing milling conditions to preserve the textural properties of activated carbon while enhancing its structural uniformity and surface reactivity. These variations are reflected in the N_2 adsorption isotherms at −196 °C (Fig. 3a–d), which correspond to BC, activated, ball-milled, and chemically pretreated samples. Based on IUPAC classification, the nitrogen adsorption isotherms at low relative pressures (P/P_0) correspond to type IV, indicative of materials containing narrow micropores, where micropore filling dominates. This classification suggests the presence of both micro- and mesopores, with interactions between gas molecules and mesopore surfaces leading to capillary condensation. Furthermore, H4-type hysteresis loops are observed at a P/P_0 of around 0.4,[62] providing further insight into pore structure modifications. The PSD analysis in Fig. 3e highlights significant variations among the samples. BC exhibits larger pores, whereas chemically and mechanically treated AC samples are characterized by micropores and mesopores.

3.3 CO_2 adsorption

CO_2 adsorption isotherms were recorded at 0 °C and are shown in Fig. 4. The CO_2 adsorption capacities of activated

Table 2 Surface area, total pore volume and CO_2 adsorption capacity of the carbon samples

Sample	S_{BET} (m^2 g^{-1})	Average pore radius (nm)	V_t (cm^3 g^{-1})	V_{mic} (cm^3 g^{-1})	V_{mes} (cm^3 g^{-1})	Adsorption capacity at 0 °C (mmol g^{-1})	Yield (%)
BC	3	8.25	0.012	0.0008	0.012	0.45	33.48
n-BC	47	3.73	0.088	0.023	0.066	0.87	—
T-BC	248	2.72	0.339	0.095	0.244	1.58	21.15
n-T-BC	201	2.22	0.224	0.085	0.139	1.47	—
AC1:1	164	4.76	0.391	0.068	0.323	2.61	20.13
n-AC1:1	65	3.47	0.114	0.034	0.080	0.62	—
T-AC1:1	711	1.48	0.528	0.298	0.230	3.50	21.02
n-T-AC1:1	240	1.48	0.179	0.099	0.079	5.14	—
AC1:2	124	6.03	0.377	0.042	0.334	0.51	7.63
n-AC1:2	20	8.51	0.086	0.007	0.079	0.28	—
T-AC1:2	924	1.37	0.637	0.334	0.303	0.29	14.85
n-T-AC1:2	458	1.37	0.315	0.157	0.158	1.46	—
AC1:3	112	5.43	0.306	0.036	0.270	0.23	5.09
n-AC1:3	9	7.57	0.037	0.003	0.034	0.46	—

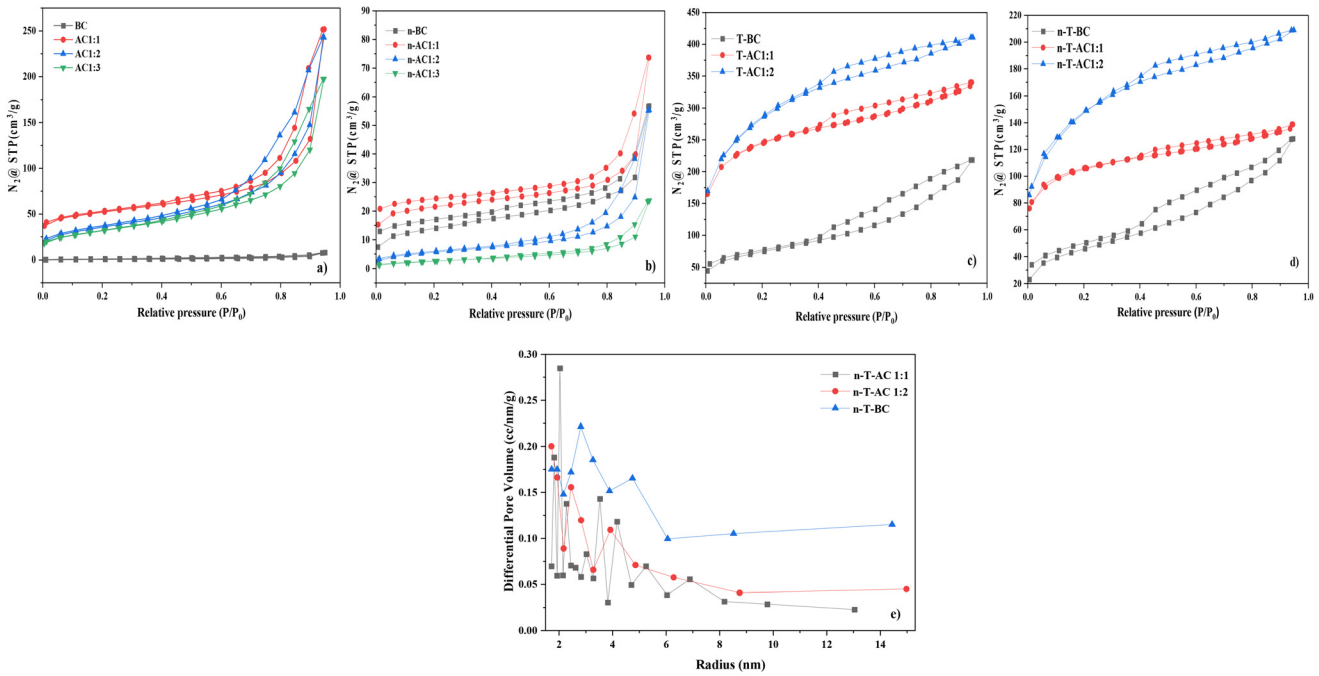

Fig. 3 N_2 adsorption–desorption isotherms of SW derived BC and AC: (a) before mechanical processing, (b) after mechanical processing, (c) after only chemical treatment, and (d) after chemical treatment followed by mechanical processing; and (e) BJH pore size distributions.

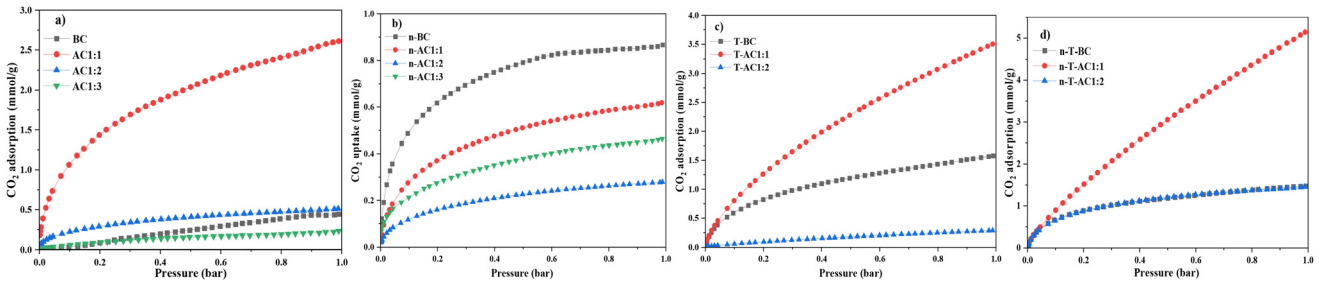

Fig. 4 CO_2 adsorption isotherms at 0 °C and 1 bar of (a) samples before mechanical processing; (b) samples after mechanical processing; (c) samples subjected to chemical treatment alone; and (d) samples subjected to chemical treatment followed by mechanical processing.

sorbent samples ranged from 0.23 to 5.14 mmol g^{-1} at 0 °C under 1 bar. Among all samples, the n-T-AC1:1 sample exhibited the highest CO_2 adsorption capacity, while the AC1:3 sample showed the lowest, as summarized in Table 2. The n-T-AC1:1 sample, prepared with an SW to KOH activation ratio of 1 : 1, was treated with HCl, activated at 800 °C, and further processed by ball milling, yielding the highest adsorption capacity. In contrast, the AC1:3 sample, which underwent no chemical or mechanical treatment, displayed the lowest value. These findings underscore the importance of both chemical and mechanical treatments in enhancing CO_2 adsorption capacity. Additionally, the CO_2 uptake capacity of the AC samples was closely related to the presence of functional groups, specific surface area (S_{BET}), and pore volume, with higher values in these parameters corresponding to increased CO_2 adsorption.[51] Fig. 5 illustrates the comparative effects of chemical and mechanical methods on the CO_2 adsorption capacities of untreated BC and AC samples. In untreated samples, ball milling (n-samples) positively influenced CO_2 adsorption in BC (n-BC), though it had a smaller effect on AC1:3 and actually led to a decline in adsorption capacity for n-AC1:1 relative to AC1:1. Conversely, HCl treatment alone significantly increased CO_2 adsorption as seen in T-BC and T-AC1:1, compared to their untreated versions, BC and AC1:1. The combination of both HCI chemical treatment and mechanical processing (ball milling) further enhanced CO_2 adsorption, resulting in substantial improvements in samples n-T-AC1:1 and n-AC1:2 over untreated samples. This comparative analysis highlights the synergistic effects of combined treatments on optimizing CO_2 capture capacity. n-T-AC1:1 was selected as the optimized sample for further studies.

The n-T-AC1:1 sample, synthesized through HCl treatment followed by ball milling, achieved a CO_2 adsorption capacity of

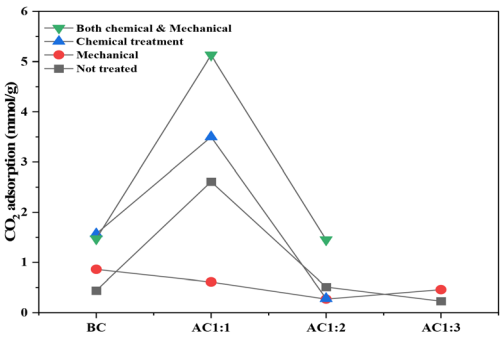

Fig. 5 Effect of chemical and mechanical methods on CO_2 adsorption of BC and AC samples at 0 °C and 1 bar.

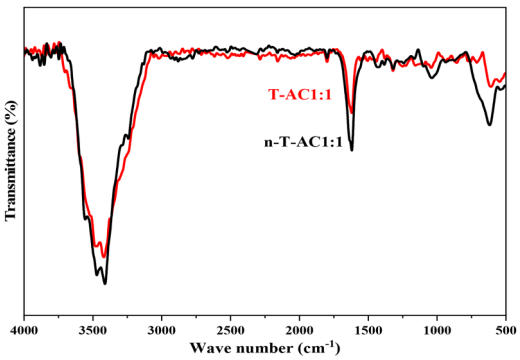

Fig. 6 FT-IR spectra of T-AC1:1 and n-T-AC1:1.

5.14 mmol g^{-1} at 0 °C and 1 bar. As highlighted in Table 3, this performance is moderate compared to previously reported materials yet notably achieved without additional ball milling optimization or surface doping. This highlights the practical potential of our approach using seafood waste as a sustainable precursor. Given its promising performance and reproducibility, n-T-AC1:1 was considered the most effective formulation in this study and forms a compelling basis for further development in carbon capture technologies.

3.4 FT-IR analysis

FTIR analysis was employed to examine the surface functional groups of the optimized sample (n-T-AC1:1) relative to the unmilled counterpart (T-AC1:1), as shown in (Fig. 6). Both spectra exhibit prominent bands characteristic of oxygen-containing groups. A broad absorption in the range of 3100–3500 cm^{-1} corresponds to –OH stretching vibrations, which may arise from hydroxyl and carboxylic acid groups or water.[67,68] Notably, the n-T-AC1:1 sample shows enhanced peak intensities at ~2900 cm^{-1} (C–H stretching) and in the region from 1750 to 500 cm^{-1}, associated with C=C, C=O, and C–H deformation vibrations,[45] indicating increased aromaticity and functionalization. These spectral enhancements suggest that ball milling facilitates surface oxidation processes, leading to a greater concentration of oxygenated functional groups. This finding is consistent with Wannasen *et al.*[69] and helps explain the significantly higher CO_2 adsorption capacity observed for n-T-AC1:1 (5.14 mmol g^{-1}) compared to T-AC1:1 (3.50 mmol g^{-1}), despite its reduced surface area (240.4 m^2 g^{-1}) compared to T-AC1:1 (711.9 m^2 g^{-1}). Previous studies[70,71] have similarly concluded that surface chemistry, with a focus on the abundance and accessibility of oxygenated groups, may exert a more dominant influence on CO_2 adsorption behavior compared to the surface area or pore volume.

3.5 Zeta potential

The zeta potential analysis further confirms the chemical modifications observed in the FTIR spectra of the optimized n-T-AC1:1 sample. As shown in Fig. 7, notable shifts in surface charge were observed across untreated and treated biochar samples. In general, the untreated BC exhibited a highly negative zeta potential of −23.265 mV, which became less negative (−12.216 mV) after ball milling. In contrast, HCl-treated biochar T-BC exhibited a strongly positive zeta potential

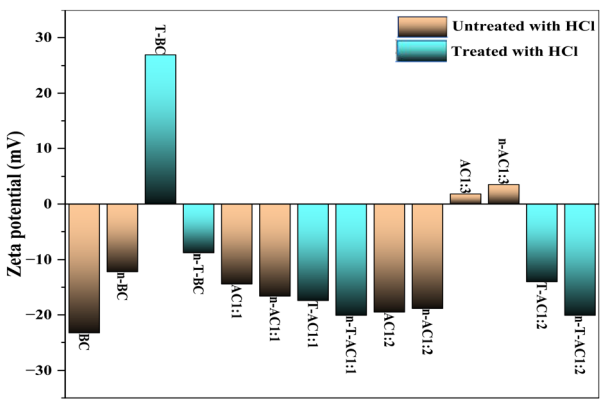

Fig. 7 Zeta potentials of BC and AC samples.

Table 3 CO_2 adsorption capacities of carbon-based materials reported in the literature

Precursor	CO_2 adsorption capacity (mmol g^{-1})	Temperature (°C)	Pressure (bar)	Ref.
Shrimp waste	5.14	0	1	This work
Cupuassu shell	7.8	0	1	63
Cashew nutshells	4.011	2525	110	64
Garlic peel	4.22	25	1	37
Black locust	5.9	0	1	65
Olive pruning waste	5.1	0	1	66
Rice husk	3.13	0	1	33

(+26.892 mV), reflecting a substantial shift in surface chemistry. This observation aligns with those of Han *et al.*,[72] demonstrating that HCl modification enhances porosity and modifies surface charge in biochar. Correspondingly, the specific surface area increased from 3 m^2 g^{-1} in raw BC to 248 m^2 g^{-1} after acid treatment. To validate these findings, EDS analysis (Fig. 8) confirmed the removal of inorganic residues and an increase in carbon content after acid treatment. Interestingly, ball milling reversed the zeta potential of T-BC from positive to moderately negative (−8.84 mV), indicating the reintroduction of acidic functional groups, as supported by the literature.[73] Similarly, for activated carbon samples, the zeta potential became more negative after ball milling: from −14.44 mV in T-AC1:1 to −16.63 mV in n-T-AC1:1. The optimized sample (n-T-AC1:1) exhibited the most negative zeta potential (−20.10 mV), compared to the non-milled T-AC1:1 sample (−17.00 mV), suggesting a higher density of surface oxygen-containing groups, such as hydroxyl and carboxyl. These negatively charged functional groups enhance electrostatic interactions with CO_2 molecules, facilitating physisorption and compensating for the reduced surface area. This relationship between surface charge and CO_2 capture efficiency is consistent with previous studies[74] and highlights the critical role of surface chemistry in adsorption behavior.

Overall, the progression in zeta potential confirms the effectiveness of chemical activation and ball milling in tailoring surface properties for improved CO_2 adsorption performance.

3.6 FE-SEM and EDS analysis

The comparative effects of HCl treatment and ball milling on the surface morphology and elemental composition of biochar samples were investigated using Field Emission Scanning Electron Microscopy (FE-SEM) and Energy Dispersive X-ray Spectroscopy (EDS). As shown in Fig. 8a, the untreated BC sample exhibits large, flaky particles with an average size of approximately 10 μm, reflecting the unmodified and compact structure of raw biochar. Following acid treatment (Fig. 8b), EDS analysis revealed a significant decrease in T-BC inorganic elements of Ca, Mg, Cl, and P. Specifically, Ca decreased from 21.7 wt% to 2.3 wt%, Mg from 1.2 wt% to 0.5 wt%, Cl from 5.4 wt% to 3.9 wt%, and P from 5.9 wt% to 0.4 wt%. These reductions confirm the efficiency of acid washing in removing surface inorganics and impurities.[72] Subsequent activation with KOH and ball milling led to further morphological transformation. In Fig. 8c, the T-AC1:1 sample shows a more open porous framework, while the n-T-AC1:1 sample (Fig. 8d) exhibits a compact, spherical morphology with an average particle size reduced to approximately 500 nm, indicative of structural refinement induced by mechanical treatment.

EDS results of T-BC also revealed a near doubling of carbon content, accompanied by sharp reductions in inorganic residues, confirming the synergy of chemical and mechanical treatments. These findings are consistent with the zeta potential and FTIR results, both of which demonstrate increased surface charge and functionalization. Collectively, these structural and compositional changes directly support the improved CO_2 adsorption performance observed in the optimized n-T-AC1:1 sample.

3.7 CO_2 Adsorption studies of the optimized sample

3.7.1 Adsorption isotherm models. To identify the isotherm model that best describes the interaction between the adsorbent and CO_2 molecules, five well-established isotherm models were fitted to the experimental data using nonlinear regression with the Solver Add-in in Microsoft Excel. The fitting accuracy was evaluated based on R^2, which reflects the degree of agreement between experimental data and the respective models,[75] as presented in Fig. 9. Among the models tested, the Freundlich model exhibited a near-perfect fit at 0 °C (R^2 = 0.9999), effectively capturing the non-uniform energy distribution and multilayer adsorption typically associated with heterogeneous surfaces.[76] Meanwhile, the Redlich–Peterson model showed strong performance across all temperatures, especially at 25 °C and 40 °C, with R^2 values of 0.9998 and 0.9999, respectively. Its hybrid nature bridging both Langmuir and Freundlich behaviors makes it particularly versatile in representing monolayer and multilayer adsorption over a wide range of operating conditions. The model ranking based on R^2 values was as follows: 0 °C: Freundlich > Redlich–Peterson > Sips > Toth > Langmuir

25 °C: Redlich–Peterson > Toth > Freundlich > Sips > Langmuir

40 °C: Redlich–Peterson > Sips > Toth > Langmuir > Freundlich

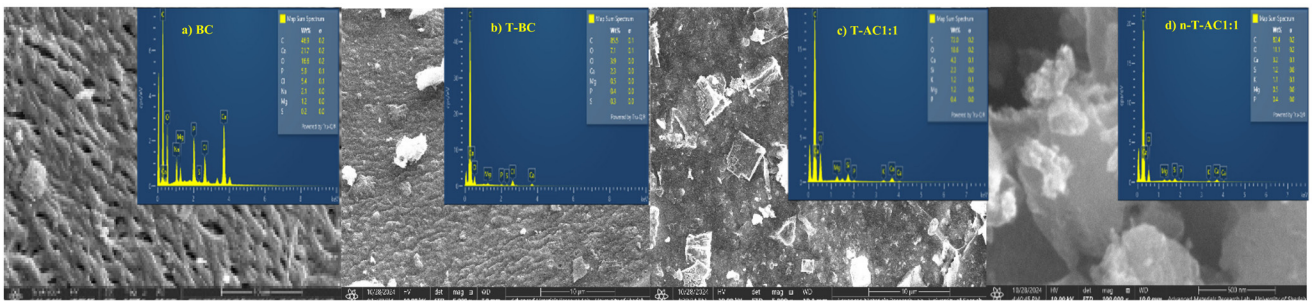

Fig. 8 SEM micrographs and EDS spectra of biochar samples showing structural and elemental changes after HCl treatment, KOH activation, and ball milling: (a) BC, (b) T-BC, (c) T-AC1:1, and (d) n-T-AC1:1.

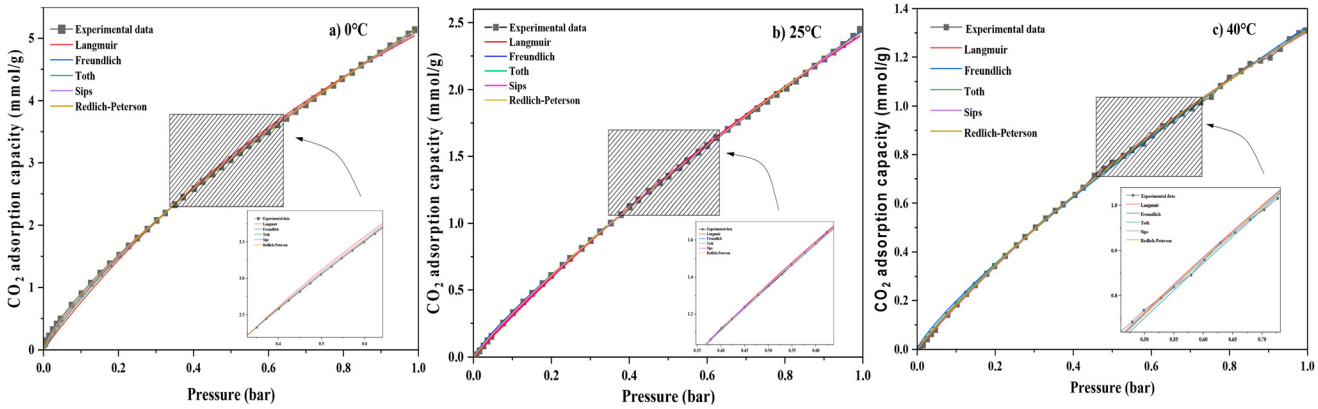

Fig. 9 CO_2 adsorption isotherm model for n-T-AC1:1 at 0 °C, 25 °C, and 40 °C.

This progressive shift in model dominance reflects a change in the adsorption mechanism with temperature. At 0 °C, the strong fit of the Freundlich and Redlich–Peterson models highlights the influence of surface heterogeneity and multilayer adsorption for the n-T-AC1:1 sample, which was synthesized through HCl treatment, KOH activation (ratio 1 : 1), and mechanical ball milling. While the milling process was not optimized for uniformity, it effectively reduced particle size and increased the exposure of active sites, contributing to the observed heterogeneous surface behavior.[77] As temperature increased, the Redlich–Peterson model became dominant, suggesting the activation of more energetically uniform sites and a shift toward a mixed-mode adsorption behavior. This transition is further supported by the reduction in maximum CO_2 adsorption capacity (q_m) with rising temperature, as determined by the Langmuir, Toth, and Sips models (Table 4), confirming the exothermic nature of the adsorption process. The temperature sensitive trend aligns with thermodynamic principles, where increased thermal energy reduces the affinity of CO_2 for the adsorbent surface. Despite the excellent fitting quality of the Langmuir model with $R^2 > 0.997$, the predicted theoretical maximum capacity of 13.7 mmol g^{-1} at 0 °C considerably exceeds the experimentally measured uptake of 5.14 mmol g^{-1}. This discrepancy reflects the heterogeneous nature of the adsorbent surface, as indicated by the relatively low Redlich–Peterson β values (0.28–0.70) and Freundlich $1/n$ values (~1.2–1.3), suggesting deviations from ideal monolayer adsorption. These observations imply that multilayer adsorption and surface heterogeneity significantly contribute to the CO_2 adsorption behavior of the n-T-AC1:1 sample. The overall isotherm behavior aligns well with the physicochemical changes introduced during material preparation. HCl pretreatment effectively removed inorganic residues (*e.g.*, Ca, Mg, Cl, and P), KOH activation generated a well-developed porous structure, and ball milling despite not being optimized enhanced surface exposure while inducing local structural irregularities. Together, these treatments produced a highly heterogeneous surface, both chemically and texturally, which explains the superior performance of the Freundlich and Redlich–Peterson models. Thus, the selected isotherm fits are not only statistically robust but also mechanistically insightful. They provide a deeper understanding of how structural vari-

Table 4 CO_2 adsorption isotherms: two-parameter and three-parameter models

CO_2 adsorption two-parameter isotherms on n-T-AC1:1						
	Langmuir			Freundlich		
Temperature (°C)	q_m	K_L	R^2	K_f	n_f	R^2
0	13.7	0.59	0.9978	5.2	1.31	0.9999
25	10.6	0.29	0.9995	2.4	1.16	0.9998
40	4.5	0.40	0.9995	1.3	1.21	0.9989

CO_2 adsorption three-parameter isotherms on n-T-AC1:1												
Toth					Sips				Redlich–Peterson			
(°C)	K_t	n_T	q_m	R^2	K_s	n_s	q_m	R^2	K_{RP}	β_{RP}	a_{RP}	R^2
0	1.94	0.69	5.1	0.9991	0.16	1.18	29.3	0.9995	42.48	0.28	7.22	0.9999
25	1.76	0.53	2.2	0.9998	0.21	1.04	13.3	0.9997	4.51	0.35	0.85	0.9998
40	1.74	0.61	1.3	0.9996	0.34	1.02	5.0	0.9996	2.03	0.70	0.55	0.9999

ation and functional group distribution influence adsorption dynamics. These findings further validate the adopted synthesis strategy and confirm the material's suitability for effective CO_2 capture.

3.7.2 Adsorption thermodynamics. The determination of thermodynamic parameters is critically linked to the interactions between CO_2 molecules and the active adsorption sites on the adsorbent surface during the adsorption process.[78] These parameters, derived from the Van't Hoff equation (eqn (4), section 2.8), are summarized in Table 5. To validate the thermodynamic values, the Van't Hoff relationship was employed *via* a plot of $\ln K_d$ *versus* $1/T$ (Fig. 10), showing excellent linearity (R^2 = 0.9819). From the slope and intercept of this plot, the enthalpy ($\Delta H°$) and entropy ($\Delta S°$) of adsorption were calculated. The negative enthalpy value ($\Delta H°$ = −23.63 kJ mol^{-1}) indicates an exothermic process, reflecting a moderate level of interaction between CO_2 and the adsorbent surface.[79,80] Moreover, the gradual decrease in the negativity of $\Delta G°$ with increasing temperature from −3.74 to −0.72 kJ mol^{-1} between 0 °C and 40 °C further supports the characteristic temperature dependence of physisorption, where adsorption weakens as thermal energy increases due to van der Waals forces.[81] In parallel, the entropy change $\Delta S°$ also shows a negative value, suggesting reduced molecular randomness during the adsorption process.[54] Taken together, $\Delta G°$, $\Delta H°$, and $\Delta S°$ along with the linear Van't Hoff analysis confirm that CO_2 adsorption onto the synthesized carbon material is exothermic, spontaneous, and governed by a physisorption mechanism under the investigated conditions.

Table 5 Thermodynamic parameters for CO_2 adsorption on the optimized sample (n-T-AC1:1)

$\Delta H°$ (kJ mol^{-1})	$\Delta S°$ (kJ mol^{-1} K)	$\Delta G°$ (kJ mol^{-1})		
		0 °C	25 °C	40 °C
−23.63	−0.07	−3.74	−2.24	−0.72

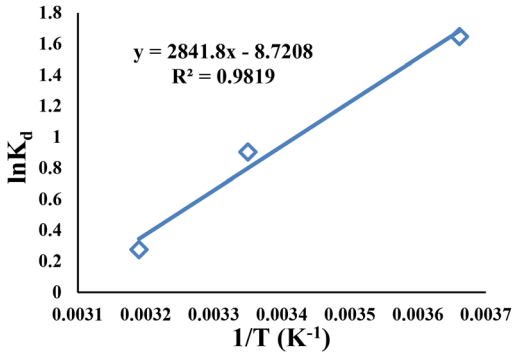

Fig. 10 Van't Hoff plot of CO_2 adsorption on n-T-AC1:1.

3.7.3 Isosteric heats of adsorption and regeneration. The surface affinity of the prepared activated carbons toward CO_2 molecules was evaluated by calculating the isosteric heat of adsorption (Q_{st}) using the Clausius–Clapeyron equation based on adsorption isotherms obtained at 0, 25, and 40 °C, as expressed in eqn(6):[82]

$$-\frac{Q_{st}}{R} = \left(\frac{\partial \ln P}{\partial T^{-1}}\right)_n \quad (6)$$

Q_{st} represents the thermal energy released during CO_2 capture, serving as a fundamental parameter for characterizing adsorption strength and providing insights into the underlying adsorption mechanism.[83] For the optimized n-T-AC1:1 sample, the overall calculated Q_{st} values fall within the range of 29.9–39.6 kJ mol^{-1}, indicating a predominantly physisorption process.[84] Values below 40 kJ mol^{-1} suggest weak to moderate interactions, mainly facilitated by dipole–quadrupole attractions between CO_2 molecules and the surface functional groups.[85] The Q_{st} trend initially exhibited a high value at low CO_2 coverage due to strong interactions within micropores, followed by a decrease as lower-energy sites were occupied, consistent with heterogeneous surface behavior described by the Freundlich model.[86–88] As depicted in Fig. 11a, the Q_{st} value shows a decreasing trend after the initial high value, and it

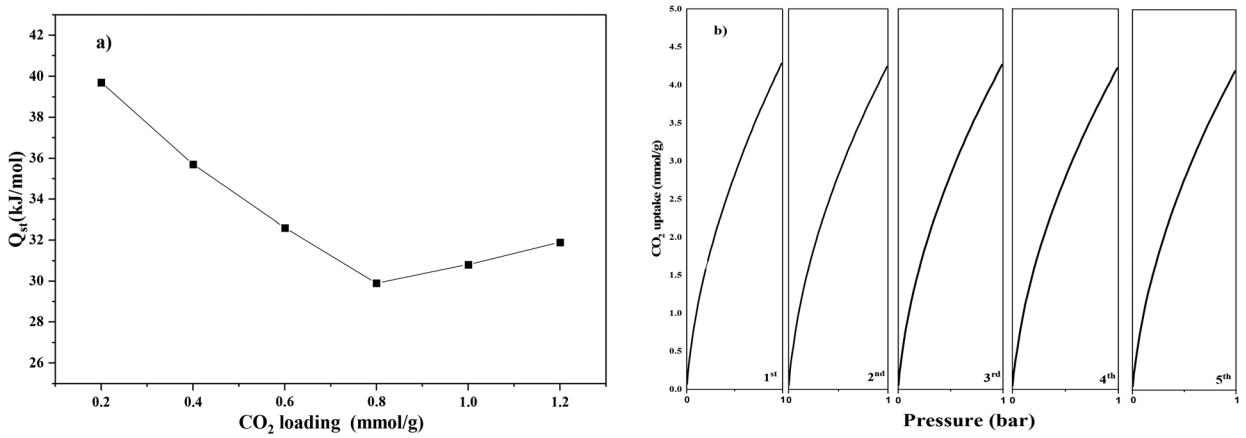

Fig. 11 Isosteric heat of CO_2 adsorption (a) and recyclability test after six months of production (b) for n-T-AC1:1.

becomes nearly uniform, indicating that the surface of the n-T-AC1:1 sample is heterogeneous in nature. The relatively high value of Q_{st}t at low CO_2 coverage is due to the CO_2 adsorption in micropores and the strong adsorbate–adsorbent interaction between CO_2 molecules and the adsorbent surface.[88] Furthermore, Q_{st} not only quantifies interaction strength but also serves as a key indicator for evaluating the adsorption mechanism and the regeneration feasibility of the adsorbent.[75,78,89]

The optimized n-T-AC1:1 also exhibited excellent regeneration stability, maintaining nearly constant CO_2 uptake over five consecutive adsorption–desorption cycles (~2.1% loss; 4.241 ± 0.016 mmol g^{-1}). To maintain transparency and demonstrate long-term performance, the same sample was remeasured after six months of storage under ambient laboratory conditions. As shown in (Fig. 11b), the cyclic CO_2 adsorption performance remained highly stable, confirming the material's strong structural resilience. The CO_2 uptake showed minimal deviation from the original performance, highlighting the adsorption durability of the material over time. The moderate Q_{st} values align well with the regeneration behaviour, as physisorption inherently promotes energetically favourable and reversible adsorption–desorption processes.[90] Together, the Q_{st} profile and cycling results consistently demonstrate that n-T-AC1:1 is a recyclable material with promising potential for sustainable CO_2 capture.

4. Conclusions

This study successfully demonstrates the synthesis of high-performance CO_2 adsorbents from shrimp waste-derived biochar through a structured process involving HCl pretreatment, KOH activation, and ball milling. The optimized sample, n-T-AC1:1, achieved a CO_2 uptake of 5.14 mmol g^{-1} at 0 °C and 1 bar, underscoring its potential for carbon capture applications. Nonlinear adsorption modeling revealed multilayer adsorption at 0 °C (Freundlich model) and a hybrid adsorption mechanism at higher temperatures (25 °C and 40 °C, Redlich–Peterson model). Thermodynamic analysis confirmed that CO_2 adsorption is spontaneous, exothermic, and dominated by physisorption, as further supported by the moderate Q_{st} values ranging from 29 to 39 kJ mol^{-1}. In addition to its adsorption capacity, the material demonstrated excellent regeneration stability over multiple adsorption–desorption cycles, further validating the reversible physisorption mechanism and long-term stability of the adsorbent. These findings confirm the effectiveness of the combined chemical and mechanical treatments in enhancing both textural and chemical properties for sustainable carbon capture. Future research should focus on evaluating CO_2 selectivity under mixed-gas environments, optimizing cycling stability under dynamic flow conditions and conducting techno-economic assessments to support industrial-scale deployment. This work establishes a promising foundation for valorizing shrimp waste into functional carbon materials, contributing to waste reduction, climate change mitigation, and circular economy initiatives.

Author contributions

Haif Aljomard: writing – original draft, investigation, data curation, resources, and conceptualization. Omar Awayssa: investigation and data curation. Chaouki Ghenai: writing – review & editing, supervision, and conceptualization.

Data availability

The data supporting the findings of this study are available upon request from the corresponding author.

Conflicts of interest

There are no conflicts to declare.

Acknowledgements

The authors sincerely acknowledge the support from the Advanced Materials Research Laboratory at the University of Sharjah for their expertise and assistance in material characterization.

References

1 J. Tkaczewska, P. Kulawik, E. Jamróz, M. Čagalj, R. F. Matas and V. Šimat, *J. Sci. Food Agric.*, 2024, **104**, 707–715.
2 Y. Chen, P. Luo, C. Hu and C. Ren, *J. Ocean Univ. China*, 2015, **14**, 484–490.
3 A. K. Wani, N. Akhtar, T. G. Mir, F. Rahayu, C. Suhara, A. Anjli, C. Chopra, R. Singh, A. Prakash, N. El Messaoudi and C. D. Fernandes, *Environ. Sci. Pollut. Res.*, 2024, **31**, 38960–38989.
4 N. Rossi, C. Grosso and C. Delerue-Matos, *Mar. Drugs*, 2024, **22**, 153.
5 Abuzar, H. R. Sharif, M. K. Sharif, R. Arshad, A. Rehman, W. Ashraf, A. Karim, K. A. Awan, H. Raza, W. Khalid, T. O. Asar and M. A. Al-Sameen, *Int. J. Food Prop.*, 2023, **26**, 3407–3432.
6 M. S. Benhabiles, N. Abdi, N. Drouiche, H. Lounici, A. Pauss, M. F. A. Goosen and N. Mameri, *Food Hydrocolloids*, 2013, **32**, 28–34.
7 M. Djellouli, M. E. López-Caballero, M. Y. Arancibia, N. Karam and O. Martínez-Alvarez, *Waste Biomass Valorization*, 2020, **11**, 2491–2505.
8 R. Susetyaningsih, S. Suntoro, T. Gunawan and M. T. S. Budiastuti, *AIP Conf. Proc.*, 2020, **2296**, DOI: 10.1063/5.0030551.

9 Z. Liu, Q. Liu, D. Zhang, S. Wei, Q. Sun, Q. Xia, W. Shi, H. Ji and S. Liu, *Foods*, 2021, **10**, 2603.
10 Y. W. S. Nair, J. Gagnon, C. Pelletier, N. Tchoukanova, J. Zhang, H. S. Ewart, K. V. Ewart and G. Jiao, *Appl. Physiol., Nutr., Metab.*, 2017, **42**, 841–849.
11 M. Nikoo, X. Xu, J. M. Regenstein and F. Noori, *Food Biosci.*, 2021, **39**, 100844.
12 X. Mao, N. Guo, J. Sun and C. Xue, *J. Cleaner Prod.*, 2017, **143**, 814–823.
13 G. M. Mathew, D. C. Mathew, R. K. Sukumaran, R. Sindhu, C. C. Huang, P. Binod, R. Sirohi, S. H. Kim and A. Pandey, *Environ. Pollut.*, 2020, **267**, 115656.
14 J. Gómez-Estaca, P. Montero and M. C. Gómez-Guillén, *J. Food Sci. Technol.*, 2018, **55**, 3881–3891.
15 K. A. Zakaria, N. I. Yatim, N. Ali, F. Lananan and N. A. Kasan, *J. Aust. Ceram. Soc.*, 2024, **60**, 1019–1029.
16 Z. Yang, Y. Zhou, H. Cui, Z. Cheng and Z. Zhou, *Front. Chem. Sci. Eng.*, 2025, **19**(9), DOI: **10.1007/s11705-024-2512-3**.
17 M. Rinaudo, *Prog. Polym. Sci.*, 2006, **31**, 603–632.
18 A. B. Jadhav and A. D. Diwan, *Indian J. Geo-Mar. Sci.*, 2018, **47**, 674–680.
19 T. S. Frantz, B. S. de Farias, V. R. M. Leite, F. Kessler, T. R. Cadaval Jr and L. A. de A. Pinto, *J. Cleaner Prod.*, 2020, **269**, 122397.
20 S. M. Pourmortazavi, H. Sahebi, H. Zandavar and S. Mirsadeghi, *Composites, Part B*, 2019, **175**, 107130.
21 R. Kazemi, A. Ronaghi, J. Yasrebi, R. Ghasemi-Fasaei and M. Zarei, *J. Soil Sci. Plant Nutr.*, 2019, **19**, 758–770.
22 A. Tarafdar and G. Biswas, *Int. J. Theor. Appl. Res. Mech. Eng.*, 2013, 17–24.
23 M. N. H. Sani, M. Amin, A. B. Siddique, S. O. Nasif, B. B. Ghaley, L. Ge, F. Wang and J. W. H. Yong, *Sci. Total Environ.*, 2023, **905**, 166881.
24 N. Chausali, J. Saxena and R. Prasad, *J. Agric. Food Res.*, 2021, **5**, 100191.
25 S. Muhammad, H. P. S. Abdul Khalil, S. Abd Hamid, Y. M. Albadn, A. B. Suriani, S. Kamaruzzaman, A. Mohamed, A. A. Allaq and E. B. Yahya, *Agriculture*, 2022, **12**, 1737.
26 A. Sharma, R. K. Sharma, Y. K. Kim, H. J. Lee and K. M. Tripathi, *J. Environ. Chem. Eng.*, 2021, **9**, 106656.
27 C. Xu, M. Nasrollahzadeh, M. Selva, Z. Issaabadi and R. Luque, *Chem. Soc. Rev.*, 2019, **48**, 4791–4822.
28 W. A. W. Mahari, K. Waiho, E. Azwar, H. Fazhan, W. Peng, S. D. Ishak, M. Tabatabaei, P. N. Y. Yek, F. Almomani, M. Aghbashlo and S. S. Lam, *Chemosphere*, 2022, **288**, 132559.
29 M. Kumar, X. Xiong, Z. Wan, Y. Sun, D. C. W. Tsang, J. Gupta, B. Gao, X. Cao, J. Tang and Y. S. Ok, *Bioresour. Technol.*, 2020, **312**, 123613.
30 T. Xing, J. Sunarso, W. Yang, Y. Yin, A. M. Glushenkov, L. H. Li, P. C. Howlett and Y. Chen, *Nanoscale*, 2013, **5**, 7970–7976.
31 Y. Zhang, J. Lu, W. Huang, L. Gao, F. Zhang, M. Omran and G. Chen, *Ceram. Int.*, 2023, **49**, 10375–10383.
32 S. O. Amusat, T. G. Kebede, S. Dube and M. M. Nindi, *J. Water Process Eng.*, 2021, **41**, 101993.
33 R. Nandi, M. K. Jha, S. K. Guchhait and D. Sutradhar, *ACS Omega*, 2023, **8**, 4802–4812.
34 G. Singh, A. M. Ruban, X. Geng and A. Vinu, *Chem. Eng. J.*, 2023, **451**, 139045.
35 X. Yuan, J. Wang, S. Deng, P. D. Dissanayake, S. Wang, S. You, A. C. K. Yip, S. Li, Y. Jeong, D. C. W. Tsang and Y. S. Ok, *ACS Sustainable Chem. Eng.*, 2022, **10**, 13026–13036.
36 J. M. Monteagudo, A. Durán, M. Alonso and A. I. Stoica, *Sep. Purif. Technol.*, 2025, **352**, 127997.
37 G. G. Huang, Y. F. Liu, X. X. Wu and J. J. Cai, *New Carbon Mater.*, 2019, **34**, 247–257.
38 C. Ghenai, K. Alamara and A. Inayat, *Energy Procedia*, 2019, **159**, 123–129.
39 C. Ghenai, M. A. Rasheed, M. J. Alshamsi, M. A. Alkamali, F. F. Ahmad and A. Inayat, *Case Stud. Therm. Eng.*, 2020, **22**, 100773.
40 X. Liu, C. He, X. Yu, Y. Bai, L. Ye, B. Wang and L. Zhang, *Powder Technol.*, 2018, **326**, 181–189.
41 L. Yang, A. Zhang and X. Zheng, *Energy Fuels*, 2009, **23**, 3859–3865.
42 S. Shao, Y. Wang, L. Ma, Z. Huang and X. Li, *Fuel*, 2024, **355**, 129287.
43 A. Ahmad, H. M. Al-Swaidan, A. H. Alghamdi, K. M. Alotaibi, M. R. Hatshan, S. Haider and I. Khan, *J. Anal. Appl. Pyrolysis*, 2024, **177**, 11–13.
44 I. A. W. Tan, A. L. Ahmad and B. H. Hameed, *J. Hazard. Mater.*, 2008, **153**, 709–717.
45 M. Raczkiewicz, I. Ostolska, O. Mašek and P. Oleszczuk, *J. Cleaner Prod.*, 2024, **458**, 20–31.
46 M. Ghaedi, *Adsorption: Fundamental Processes and Applications*, 1st edn, 2021, vol. 33.
47 E. Diaz, I. Sanchis, C. J. Coronella and A. F. Mohedano, *Resources*, 2022, **11**, 43.
48 Y. Li, G. Zhang, J. Liu, G. Li and Y. Wang, *J. Energy Inst.*, 2023, **111**, 101415.
49 K. Y. Foo and B. H. Hameed, *Chem. Eng. J.*, 2010, **156**, 2–10.
50 J. Serafin and B. Dziejarski, *Microporous Mesoporous Mater.*, 2023, **354**, 112513.
51 K. C. Bedin, A. C. Martins, A. L. Cazetta, O. Pezoti and V. C. Almeida, *Chem. Eng. J.*, 2016, **286**, 476–484.
52 F. Bouhamed, Z. Elouear and J. Bouzid, *J. Taiwan Inst. Chem. Eng.*, 2012, **43**, 741–749.
53 M. A. Al-Ghouti and D. A. Da'ana, *J. Hazard. Mater.*, 2020, **393**, 122383.
54 A. Sarwar, M. Ali, A. H. Khoja, A. Nawar, A. Waqas, R. Liaquat, S. R. Naqvi and M. Asjid, *J. CO2 Util.*, 2021, **46**, 101476.
55 F. Raganati, M. Alfe, V. Gargiulo, R. Chirone and P. Ammendola, *Chem. Eng. Res. Des.*, 2018, **134**, 540–552.
56 Y. H. Fseha, J. Shaheen and B. Sizirici, *Emerging Contam.*, 2023, **9**, 100202.
57 D. Núñez-Gómez, C. Rodrigues, F. R. Lapolli and M. A. Lobo-Recio, *J. Polym. Environ.*, 2021, **29**, 576–587.

58 L. Meng, S. Y. Foong, P. N. Y. Yek, R. K. Liew, A. M. Karami, M. Verma, N. L. Ma, C. Sonne, J. C. Lan and S. S. Lam, *Energy Environ.*, 2023, **19**, 0958305X231215317.
59 P. Zhang, H. Hu, H. Tang, Y. Yang, H. Liu, Q. Lu, X. Li, N. Worasuwannarak and H. Yao, *Renewable Energy*, 2019, **139**, 730–738.
60 A. Nasrullah, A. S. Khan, A. H. Bhat, I. U. Din, A. Inayat, N. Muhammad, E. M. Bakhsh and S. B. Khan, *Renewable Energy*, 2021, **168**, 723–733.
61 D. D. Y. Ryu, S. B Lee, T. Tassinari and C. Macy, *Biotechnol. Bioeng.*, 1982, **24**, 1047–1067.
62 R. Bardestani, G. S. Patience and S. Kaliaguine, *Can. J. Chem. Eng.*, 2019, **97**, 2781–2791.
63 O. F. Cruz, I. Campello-Gómez, M. E. Casco, J. Serafin, J. Silvestre-Albero, M. Martínez-Escandell, D. Hotza and C. R. Rambo, *Carbon Lett.*, 2023, **33**, 727–735.
64 Ó. J. Fonseca-Bermúdez, L. Giraldo, R. Sierra-Ramírez, J. Serafin, B. Dziejarski, M. G. Bonillo, G. Farid and J. C. Moreno-Piraján, *J. CO2 Util.*, 2024, **83**, 102799.
65 C. Zhang, W. Song, Q. Ma, L. Xie, X. Zhang and H. Guo, *Energy and Fuels*, 2016, **30**, 4181–4190.
66 P. B. Ramos, A. Mamaní, M. Erans, F. Jerez, M. F. Ponce, M. F. Sardella, A. Arencibia, M. A. Bavio, E. S. Sanz-Pérez and R. Sanz, *Energy and Fuels*, 2024, **38**, 6102–6115.
67 J. J. Ternero-Hidalgo, J. M. Rosas, J. Palomo, M. J. Valero-Romero, J. Rodríguez-Mirasol and T. Cordero, *Carbon*, 2016, **101**, 409–419.
68 M. Zolfi Bavariani, A. Ronaghi and R. Ghasemi, *Commun. Soil Sci. Plant Anal.*, 2019, **50**, 402–411.
69 L. Wannasen, N. Chanlek, S. Siriroj, S. Maensiri, E. Swatsitang and S. Pinitsoontorn, *Nanomaterials*, 2022, **12**, 3555.
70 W. Xing, C. Liu, Z. Zhou, J. Zhou, G. Wang, S. Zhuo and Q. Xue, *Nanoscale Res. Lett.*, 2014, 1–8.
71 J. David and E. Kopac, *J. Anal. Appl. Pyrolysis*, 2014, **110**, 322–332.
72 Y. Han, J. Zheng, C. Jiang, F. Zhang, L. Wei and L. Zhu, *J. Environ. Chem. Eng.*, 2022, **10**, 108903.
73 H. Lyu, B. Gao, F. He, A. R. Zimmerman, C. Ding, H. Huang and J. Tang, *Environ. Pollut.*, 2018, **233**, 54–63.
74 H. R. Abid, S. Iglauer, A. Al-Yaseri and A. Keshavarz, *Energy*, 2021, **233**, 120924.
75 N. A. Rashidi and S. Yusup, *J. Cleaner Prod.*, 2017, **168**, 474–486.
76 P. S. Figueiredo, L. R. Hollanda, O. Chiavone-Filho, F. A. da Costa Fa, G. L. Dotto and E. L. Foletto, *Environ. Sci. Pollut. Res.*, 2025, **32**, 8254–8266.
77 E. Partlan, K. Davis, Y. Ren, O. G. Apul, O. T. Mefford, T. Karanfil and D. A. Ladner, *Water Res.*, 2016, **89**, 161–170.
78 J. Kapica-Kozar, B. Michalkiewicz, R. J. Wrobel, S. Mozia, E. Piróg, E. Kusiak-Nejman, J. Serafin, A. W. Morawski and U. Narkiewicz, *New J. Chem.*, 2017, **41**, 7870–7885.
79 R. K. Jha, H. Bhunia and S. Basu, *Heliyon*, 2024, **10**, DOI: **10.1016/j.heliyon.2024.e27439**.
80 V. K. Singh and E. A. Kumar, *Mater. Today Proc.*, 2018, **5**, 23033–23042.
81 A. L. Myers and J. M. Prausnitz, *AIChE J.*, 1965, **11**, 121–127.
82 M. S. Khosrowshahi, H. Mashhadimoslem, H. B. M. Emrooz, A. Ghaemi and M. S. Hosseini, *Diamond Relat. Mater.*, 2022, **127**, 109204.
83 Q. Xu, J. Wang, J. Feng, C. Liu, Q. Xiao, M. Demir, U. B. Simsek, M. Kılıç, L. Wang and X. Hu, *Colloids Surf., A*, 2025, **709**, 136054.
84 T. Lu, J. Bai, J. Huang, Q. Yu, M. Demir, M. Kilic, B. N. Altay, L. Wang and X. Hu, *Energy Fuels*, 2023, **37**, 3886–3893.
85 J. Serafin, B. Dziejarski, O. F. C. Junior and J. Sreńscek-Nazzal, *Carbon*, 2023, **201**, 633–647.
86 L. Xie, Q. Li, M. Demir, Q. Yu, X. Hu, Z. Jiang and L. Wang, *Colloids Surf., A*, 2022, **655**, 130226.
87 B. González and J. J. Manyà, *Chem. Eng. Process.*, 2020, **149**, 107830.
88 J. Shao, Y. Wang, C. Liu, Q. Xiao, M. Demir, M. K. Al Mesfer, M. Danish, L. Wang and X. Hu, *J. Anal. Appl. Pyrolysis*, 2025, **186**, 106946.
89 H. Patel, H. Weldekidan, A. Mohanty and M. Misra, *Carbon Capture Sci. Technol.*, 2023, **8**, 100128.
90 C. Ma, T. Lu, M. Demir, Q. Yu, X. Hu, W. Jiang and L. Wang, *ACS Appl. Nano Mater.*, 2022, **5**, 13473–13481.